

Novel Integrated Bearingless Hollow-Shaft Drive

Thomas Schneeberger, Johann W. Kolar

Power Electronic Systems Laboratory
ETH Zurich
8092 Zurich, Switzerland
schneeberger@eek.ee.ethz.ch / kolar@lem.ee.ethz.ch

Abstract— This paper describes a novel and compact design concept for contactless levitation and rotation of a wide annular rotor through the walls of a process chamber. In the proposed set-up, a homopolar magnetic bearing biased by permanent magnets is combined with a high-pole-number segment motor. The paper describes the functional principle of the motor focusing on the design and the behavior of the drive. An experimental system is presented along with a comprehensive set of measurement results verifying the theoretical considerations.

Index Terms— Magnetic bearing, bearingless motor, hollow shaft drive, process chamber.

I. INTRODUCTION

The reproducibility of many industrial processes can be improved by the use of hermetically sealed process chambers, since they facilitate proper control of crucial process parameters such as pressure, temperature, or composition of the gas or liquid surrounding an object that is to be processed. These chambers are used in biotechnological applications [1] as well as in the semiconductor industry [2], where they also prevent leakage of potentially harmful chemicals into the environment. State-of-the-art wafer production requires a device placed inside of the sealed chamber and which rotates the wafer during processing, thereby providing a uniformly distributed concentration and flow pattern. The design of existing process chambers for wafer production relies on a gas-tight feed through of the rotating drive axis (in the wall of the process

chamber) and is, therefore, afflicted with two major disadvantages. Not only are the drive shaft, the shaft sealing, the bearings, and the motor rather bulky, sometimes occupying a significant portion of the space available inside of the chamber, but they also generate particles detrimental for the media inside of the chamber at every frictional contact between moving parts.

In this paper, a novel bearingless hollow shaft drive, which is based on the principle of the “Bearingless Motor” ([3] - [9]), is described. This drive allows for contactless levitation and rotation effectuated through the walls of the chamber on a rotor to which a wafer clamping device is attached (**Fig. 1**). Due to the entire integration of the drive and the magnetic bearing, the over-all size of the motor is significantly smaller than any design with the magnetic bearings separated from the drive. All elements necessary for the drive and bearings (coils, sensors and electronics) are placed outside the chamber and are integrated in the motor stator. Also the corresponding power and data processing electronics can be placed outside the process chamber, and is therefore not exposed to harmful process chemicals and can be replaced quickly in the case of a failure. The object to be treated is clamped in the middle of an annular rotor and the whole place in the chamber above and beneath the object remains free from any bearing or drive elements. Therefore, process sources, such as nozzles or radiation sources, can be placed on both sides of the object, which allows a simultaneous treatment of both object surfaces.

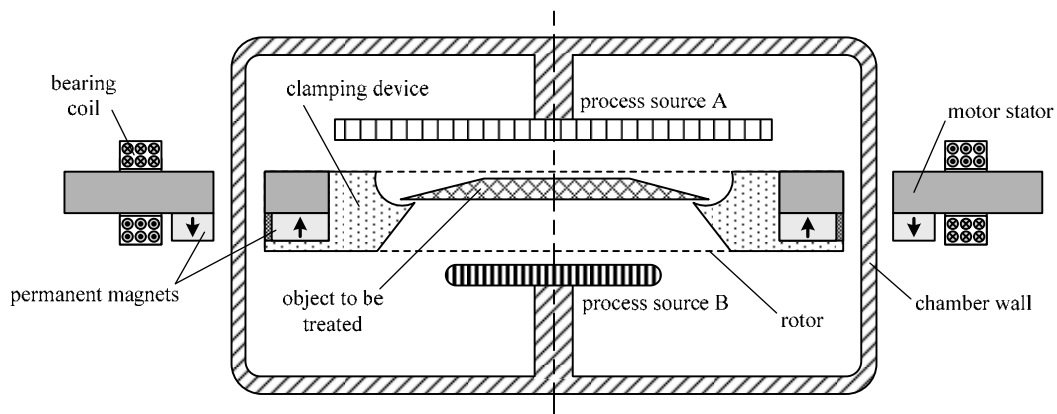


Fig. 1. Arrangement of a hermetically sealed process chamber with the proposed bearingless hollow shaft drive and two process sources. All electric parts of the system are placed outside the chamber, only the rotor floats inside the process chamber and is levitated by magnetic fields through its walls. Therefore, the rotor is easy accessible from both sides.

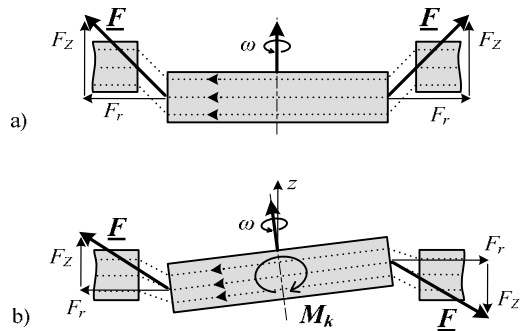


Fig. 2. (a) Axial support and (b) stabilization against tilting of the rotor by passive magnetic forces in a “Bearingless Motor” [1], [2], [9].

II. MOTOR FUNCTIONAL PRINCIPLE

A. Bearing

In principle, the rotor has six spatial degrees of freedom: linear motion and rotation along each of three axes in an xyz-system. While the rotor is held in place by the bearing, all three of its translatory modes and two of its rotatory modes of motion must be suppressed. The only remaining degree of freedom is the desired rotation around the z-axis.

In contrast to conventional magnetically levitated drives, the bearing forces in a “Bearingless Motor” are not built up in additional magnetic bearings placed along the axis of rotation, but in the motor itself. The active motor part generates the torque as well as radial magnetic bearing forces. Because the length of the rotor is small compared to its diameter, it is possible to stabilize three spatial degrees of freedom (z position, tilting moment in x and y direction) passively by attractive magnetic forces (minimization of reluctance, **Fig. 2**) so that only one active radial bearing (for x and y position) is needed. Although being stabilized only passively, the axial position of the rotor lies within a narrow range for small loads. For special applications, its accuracy could be improved by additional or stronger permanent magnets or by adjusting the axial position of the stator.

Fig. 3 shows the functional principle of the active radial bearing. Permanent magnets placed on the rotor and on the stator provide a bias flux in the air gap. Depending on the axial position of the rotor, the bearing windings are supplied with a current, which alters the flux density in the air gap, thereby generating a resulting Maxwell-force towards the target position. In order to maximize this Maxwell-force, both opposite bearing windings are connected against each other.

The use of high-energy permanent magnets to generate a magnetically biased bearing flux leads to a compact system: The neodymium iron boron magnets used in this set-up have coercive field strengths of more than 1000kA/m. As an example, a coil with 8’000 ampere turns generates the same field strength as a magnet with a height of only 8mm. However, a reasonable force on the rotor is obtainable with a comparatively low bearing current due to the square dependence of the Maxwell-force on the magnetic flux density.

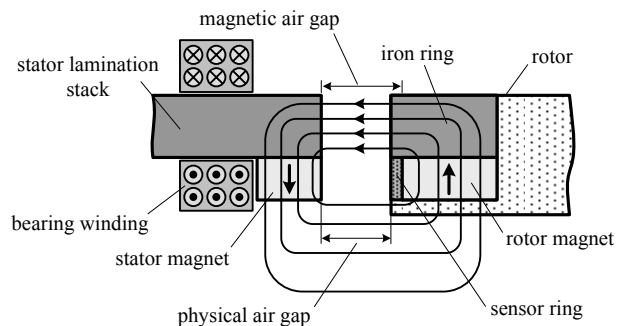


Fig. 3. Homopolar active magnetic bearing to support the axial rotor position. The bearing is biased by rare earth permanent magnets, which reduces the size of the bearing winding.

It must be noted that, due to the relative permeability of a permanent magnet, which is approximately unity, a bearing design, where (additional) permanent magnets are placed horizontally in the direction of the air gap flux, is inadvisable. In such a design, the magnetic air gap would automatically be enlarged by the size of the magnets if the physical air gap is kept constant. An enlarged air gap leads to a reduced flux density, since the flux density is inversely proportional to the gap width. This will result in a drastically reduced bearing force, since the Maxwell-force scales with flux density squared.

B. Drive

For the applications described in the introduction, only a moderate torque is required to overcome the rotor torque resulting from inertia. A rapid acceleration is crucial to ensure a reasonable cycle time. A speed range from 1rpm (for allowing a more homogeneous exposure of a process to the object) up to 1500rpm (spin cycle) must be covered. For the rotation to be uniform even at a speed as low as 1rpm, a motor configuration with a high pole number is a necessary prerequisite.

In our configuration, which was introduced earlier [1], the bearing bias magnets on the rotor are used to generate a high-pole, modulated but rectified bias flux. For this purpose, the magnets mounted on the rotor are not placed next to each other, but in pole distance (**Fig. 4**). To retain the

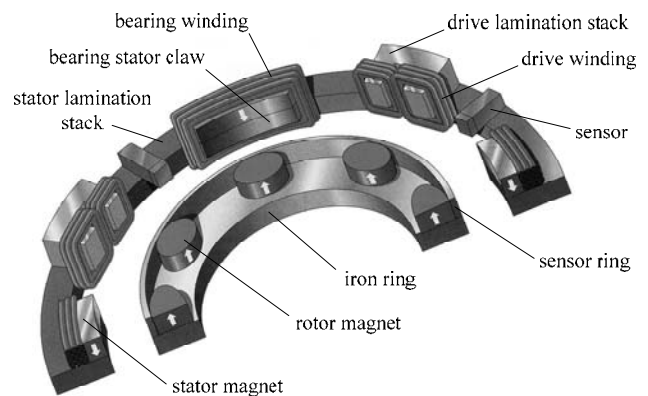


Fig. 4. Bottom stereoscopic sectional view of the hollow shaft drive. Independent of the rotor angle, always one rotor pole is in front of one stator pole. In this set-up four times two drive windings are provided.

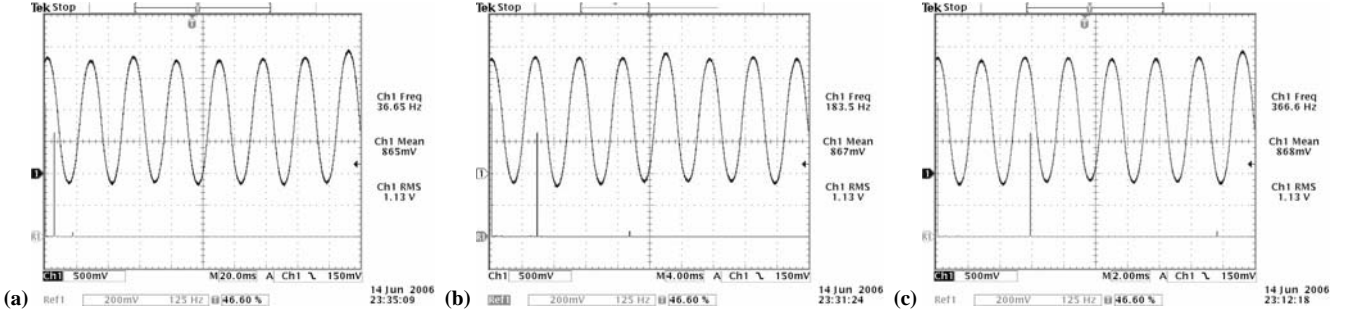


Fig. 5. The magnetic flux density B measured in the middle of a drive lamination stack (Ch1: 10mV = 1mT) and its spectrum analysis (Ref1) for (a) 100rpm ($f_{el} = 36.7\text{Hz}$), (b) 500rpm ($f_{el} = 183.3\text{Hz}$), and (c) 1000rpm ($f_{el} = 366.7\text{Hz}$). The time-dependent behavior of $B(t)$ is sinusoidal and its amplitude is speed independent of the rotor speed. Variations in the amplitudes of $B(t)$ are caused by the tolerances of the magnets.

homopolarity of the bearing, the pole width of the bearing stator claws must be matched to the pole width of the rotor. This modulated bias flux in interaction with the motor segments of the same pole width on the stator generates the torque (synchronous rotating field machine). Obviously, the maximum possible torque is limited by the size of the air gap.

For the field orientated speed control, two hall sensors - placed on the stator - determine the rotor angle in a sine-cosine analysis. For a detailed information on the current and position control procedure we refer to [7] and [10] for the sake of brevity.

III. MOTOR DESIGN ASPECTS

In this section, the basic procedure of the drive design is described. The determination of the proper number of turns of the drive coils is depicted as well as the resulting potential in motor torque and acceleration. The elementary description of the drive design is followed by an optimization procedure focused on the objective to reach a defined rotor speed as quickly as possible while considering the features of two existing motor controllers A and B (specified later).

A. Analysis of the Magnetic Circuit

Due to the complex layout of the different lamination stacks and of the permanent magnets resulting in a major ratio of leakage fields, an analytic derivation of the magnetic flux density around the drive lamination stacks is not possible. Therefore, as a base for the description of the magnetic conditions for the drive section, the voltage $u_{ind}(t)$ induced in one of the k drive coils is measured at different rotor speeds. For this measurement the rotor is driven in single-phase operation and the induced voltage is measured in the open coil(s) of the second phase. The voltage $u_{ind}(t)$ can be derived as

$$\begin{aligned} u_{ind}(t) &= N \cdot \frac{d\phi}{dt} = N \cdot \left(A \cdot \frac{dB}{dt} + B \cdot \frac{dA}{dt} \right) \\ &= N \cdot A \cdot \frac{dB}{dt}, \end{aligned} \quad (1)$$

where k is the number of drive coils, N the number of turns of one drive coil, A the cross-sectional area of the drive lamination stack, and B the magnetic flux density.

Fig. 5 shows the magnetic flux density B measured in the central point of a drive lamination stack at different rotor speeds n_R . Due to the arrangement of the permanent magnets B has a non-zero average, but its amplitudes are independent of the rotor speed. The crucial factor for the induced voltage and the motor torque, respectively, is just the alternating component of B . As a result of the large leakage fields, a homogeneous distribution of the magnetic flux density B over the entire pole face cannot be assumed; dividing the measured value $u_{ind}(t)$ by A leads, therefore, to a derivative, dB/dt , averaged over the entire pole face.

Saturation effects in this set-up are of minor importance due to the big air gap and the comparatively small number of ampere turns, even if the drive coils are supplied with the maximal drive current.

The time-dependent behavior of $B(t)$ is virtually sinusoidal as a spectrum analysis of $u_{ind}(t)$ shows in Fig. 5:

$$B(t) = \hat{B} \cdot \sin(2\pi f_{el} \cdot t). \quad (2)$$

The frequency f_{el} of the induced voltage $u_{ind}(t)$ is calculated from the rotor speed n_R (in rpm) and the number of pole pairs p of the rotor:

$$f_{el} = \frac{n_R}{60} \cdot p. \quad (3)$$

From this, the induced voltage can be derived as:

$$u_{ind}(t) = 2\pi \frac{n_R}{60} \cdot p \cdot N \cdot \hat{B} \cdot A \cdot \cos(2\pi \frac{n_R}{60} \cdot p \cdot t). \quad (4)$$

Tab. 1 shows the values of the induced voltage measured in the experimental set-up. Due to the proportionality of $U_{ind,RMS}$ and the rotor speed n_R a speed independent and al-

n_R [rpm]	f_{el} [Hz]	$U_{ind,RMS}$ [V]	$k_{U_{ind}}$ [mV/rpm]
100	36.7	0.68	6.80
200	73.3	1.30	6.50
400	146.7	2.50	6.25
600	220.0	3.75	6.25
800	293.3	4.95	6.19
1000	366.7	6.15	6.15
1200	440.0	7.35	6.13

Tab. 1. RMS-value of the induced voltage $u_{ind}(t)$ and $k_{U_{ind}}$ measured in the experimental set-up ($p = 22$) in one drive coil ($N = 190$) for different rotor speeds.

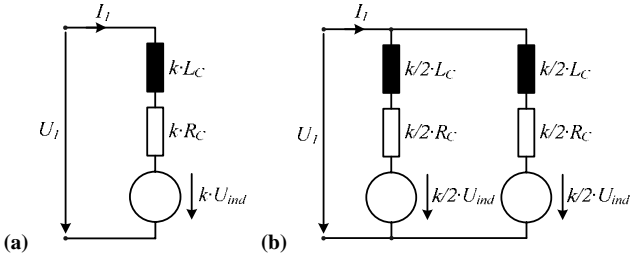


Fig. 6. Equivalent electrical circuit of one drive phase with (a) four drive coils all connected in series or (b) twice two coils connected in parallel.

most constant factor $k_{U_{ind}}$ can be calculated by averaging:

$$k_{U_{ind}} = \frac{1}{i} \cdot \sum_i \frac{U_{ind,RMS}}{n_R} \quad (5)$$

B. Equivalent Electrical Circuit of one Drive Phase

The equivalent electrical circuit consists of the above-derived induced voltage U_{ind} , of the coil resistance R_C , the coil inductivity L_C , and of the voltage source U_i . All of the k drive coils can be connected in series (**Fig. 6(a)**) or, for example, the two coils that are attached in series connection on one drive lamination stack can be connected in parallel (**Fig. 6(b)**). Applying Kirchhoff's law to the equivalent electrical circuit for the configuration with drive coils in series connection leads to

$$\underline{U}_1 = k \cdot R_C \cdot \underline{I}_1 + k \cdot j\omega_{el} L_C \cdot \underline{I}_1 + k \cdot \underline{U}_{ind}, \quad (6)$$

or for the second configuration, respectively, to:

$$\underline{U}_1 = \frac{k}{4} \cdot R_C \cdot \underline{I}_1 + \frac{k}{4} \cdot j\omega_{el} L_C \cdot \underline{I}_1 + \frac{k}{2} \cdot \underline{U}_{ind}. \quad (7)$$

The following calculations are carried out corresponding to the configuration depicted in **Fig. 6(a)**. The induced voltage is in phase with the drive current I_1 and, together with the phasor chart (see **Fig. 7(a)**), the following equation can be derived:

$$(k \cdot U_{ind} + k \cdot R_C \cdot I_1)^2 + (\omega_{el} \cdot k \cdot L_C \cdot I_1)^2 = U_1^2. \quad (8)$$

The resistance R_C of one coil is calculated applying

$$R_C = \rho \cdot (1 + \alpha \cdot (T - T_0)) \cdot \frac{N \cdot l}{(d/2)^2 \cdot \pi}, \quad (9)$$

where ρ is the resistivity, α the temperature coefficient, T

the operating temperature (e.g. 75°C), N the number of windings, l the average length of one winding, and d the wire diameter.

The inductivity L_C of a coil is given by

$$L_C = \frac{\mu \cdot N^2 \cdot A_L}{l_L}, \quad (10)$$

where $\mu = \mu_0 \cdot \mu_r$ is the permeability, N the number of windings, A_L the coil cross-sectional area, and l_L the coil length. Using (10), the drive coil inductivity L_C of this configuration cannot be calculated. However, the quadratic relation of L_C with N can be used to calculate L_C for a given number of turns N_I of the drive winding, starting from an initial coil inductivity measurement L_0 of a drive coil with a specified number of turns N_0 :

$$L_C = \frac{N_I^2}{N_0^2} \cdot L_0. \quad (11)$$

C. Drive Current and Induced Voltage Depending on the Rotor Speed and the Number of Turns of the Drive Coils

The drive current I_1 can be obtained from (8):

$$I_1 = \frac{-U_{ind} \cdot R_C \pm \sqrt{(R_C^2 + \omega_{el}^2 \cdot L_C^2) \frac{U_1^2}{k^2} - \omega_{el}^2 \cdot L_C^2 \cdot U_{ind}^2}}{R_C^2 + \omega_{el}^2 \cdot L_C^2} \quad (12)$$

With the formulas derived above, U_{ind} and I_1 (not listed) are calculated as a function of the rotor speed n_R with the optimized number of turns N_I as a parameter:

$$U_{ind} = k_{U_{ind}} \cdot n_R \cdot \frac{N_I}{N_0}. \quad (13)$$

Now, the phasor charts and the behavior of U_{ind} and I_1 can be calculated (e.g. with MATLAB) for different numbers of turns. The current limit $I_{1,max}$ and the maximum output voltage $U_{1,max}$ given by the motor controller specifications can also be taken into consideration of the drive coil design.

Fig. 7 shows the phasor charts for $N_I = N_0 = 190$ and $k = 4$ for a motor controller (type B) with a dc link voltage of $U_{DC} = 325V$ and the drive current $I_{1,RMS}$ limited to a maximum of 5.3A. **Fig. 8(a)** depicts the behavior of U_{ind} and I_1 as a function of the rotor speed n_R varying the number windings N_I .

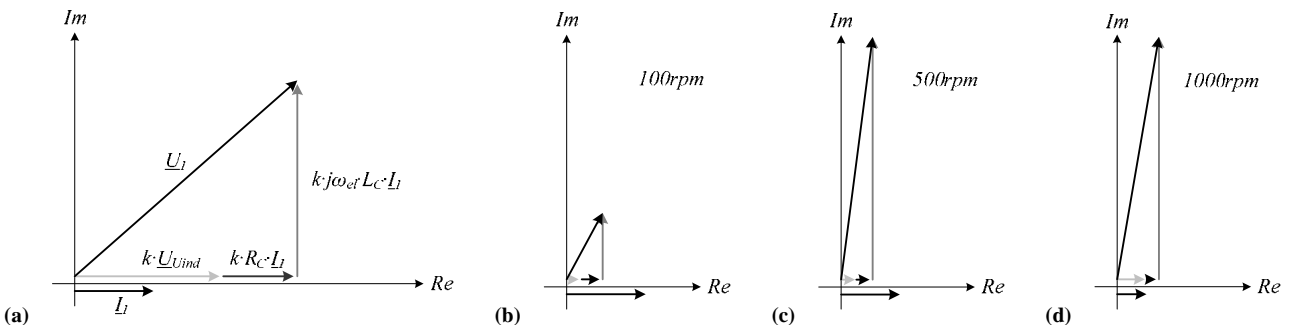


Fig. 7. (a) Phasor chart of the equivalent electrical circuit of one drive phase with the basic phasor orientation. Calculated phasor charts for $N_I = N_0 = 190$ and $k = 4$ for the motor controller B with a dc link voltage of $U_{DC} = 325V$ and a drive current limit of $I_{1,RMS} = 5.3A$ for a rotor speed of (b) 100rpm, (c) 500rpm, and (d) 1000rpm with in each case the maximal possible drive current I_1 and the maximal motor torque respectively.

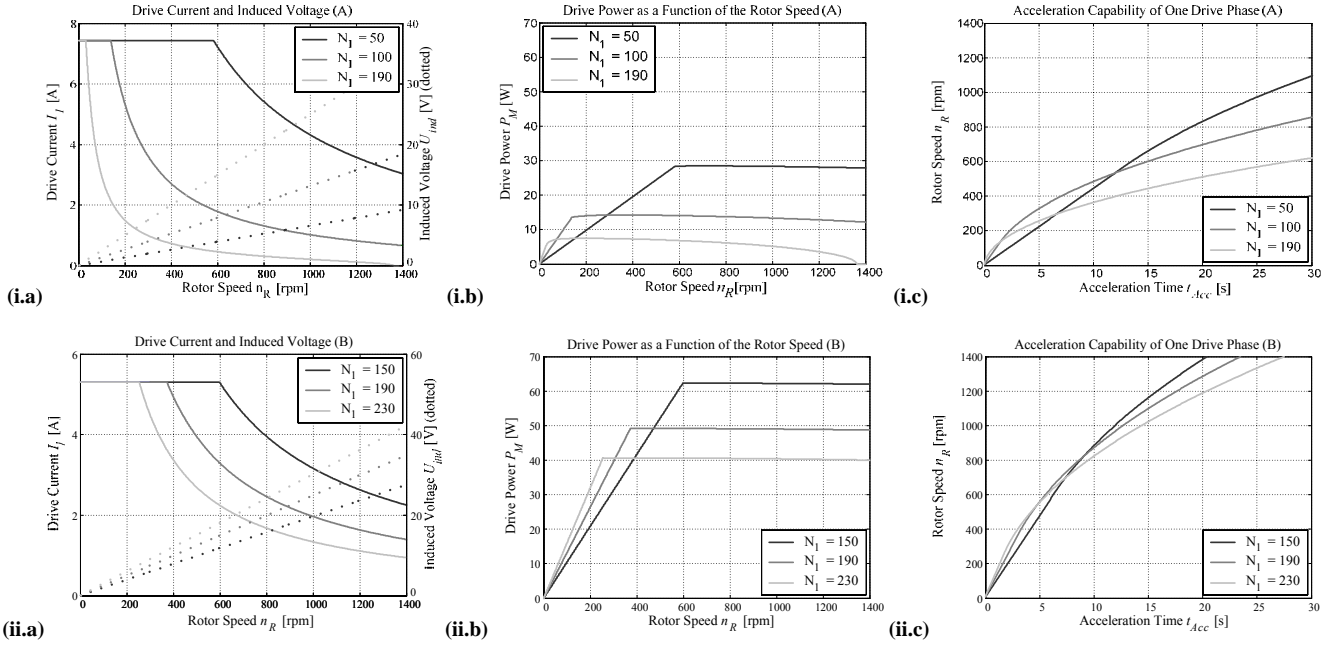


Fig. 8. Calculated characteristics of one drive phase for a dc link voltage of $U_{DC} = 48V$ and a drive current limit of $I_1 = 7.4A$ (motor controller A, (i.a-c) and for a dc link voltage of $U_{DC} = 325V$ and a drive current limit of $I_{1,RMS} = 5.3A$ (motor controller B, (ii.a-c)); (a) current and induced voltage, (b) drive power as a function of the rotor speed, and (c) acceleration capability.

D. Motor Power and Acceleration

The motor drive power P_M of one phase can be calculated on the one hand using:

$$P_M = k \cdot U_{ind} \cdot I_1 = k \cdot \frac{N_1}{N_0} \cdot k_{Uind} \cdot n_R \cdot I_1, \quad (14)$$

and on the other hand applying:

$$P_M = M_M \cdot 2\pi \cdot \frac{n_R}{60}. \quad (15)$$

Combining (15) and (16), the motor torque is directly proportional to the drive current I_1

$$M_M = \frac{60 \cdot k}{2\pi} \cdot \frac{N_1}{N_0} \cdot k_{Uind} \cdot I_1, \quad (16)$$

and therefore constant as long as I_1 is not reduced by reaching the limit of the voltage source U_1 (Fig. 8(b)).

The rotor acceleration capability is derived from the energy which is fed to the rotor within an infinitesimal time step dt

$$dE = P_M \cdot dt = k \cdot \frac{N_1}{N_0} \cdot k_{Uind} \cdot n_R \cdot I_1 \cdot dt, \quad (17)$$

leading to an acceleration of the rotor and therefore to an increased rotatory energy

$$E = \frac{1}{2} \cdot J \cdot \omega_R^2, \quad (18)$$

where J is the rotor moment of inertia in the direction of the rotation axis. Equation (19) can be transformed into

$$dE = J \cdot \left(\frac{2\pi}{60} \right)^2 \cdot n_R \cdot dn_R, \quad (19)$$

and finally, together with (18), the necessary acceleration time t_{Acc} that the rotor needs to reach a desired process speed

n_P can be computed:

$$t_{Acc} = \frac{J}{k \cdot k_{Uind}} \cdot \left(\frac{2\pi}{60} \right)^2 \cdot \frac{N_0}{N_1} \cdot \int_0^{n_P} \frac{1}{I_1(n_R)} \cdot dn_R. \quad (20)$$

Fig. 8(c) depicts the calculated values for the acceleration time depending on the number of turns of the drive coils and on the specifications of the respective motor controller.

E. Optimization of the Number of Winding Turns and Final Considerations

The calculated characteristics depicted in Fig. 8 illustrate the behavior of the drive depending on the number winding turns: A large number of turns increases the induced voltage and therefore the delivered power for acceleration. However, the large inductance combined with the high number of poles generates a large inductive voltage drop reducing the maximum possible drive current even at a comparatively low speed. Therefore the reactive power is large compared to the effective power which is obviously a result of the weak magnetic coupling due to the large width of the air gap.

Thus, the drive design requires a compromise between a large induced voltage and a small number of turns. Particularly, at low dc-link voltages, the optimization with respect to the maximum achievable acceleration leads to a moderate torque in the low-speed range (Fig. 8(c)). Besides that, an increased acceleration rate can be achieved by selecting permanent magnets with higher coercive field strengths or by reducing the air gap width. The latter of which is not applicable as an air gap width as large as possible is required in the presented case.

A first prototype of the outlined hollow shaft drive has

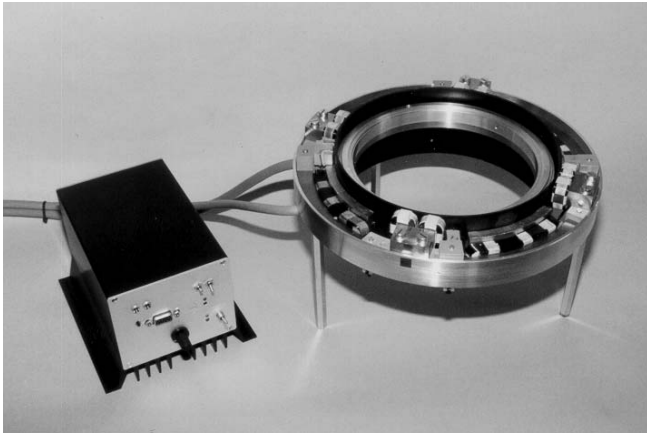


Fig. 10. Experimental set-up with an inside rotor diameter of 160mm and an air gap of 3mm, driven by the motor controller A.

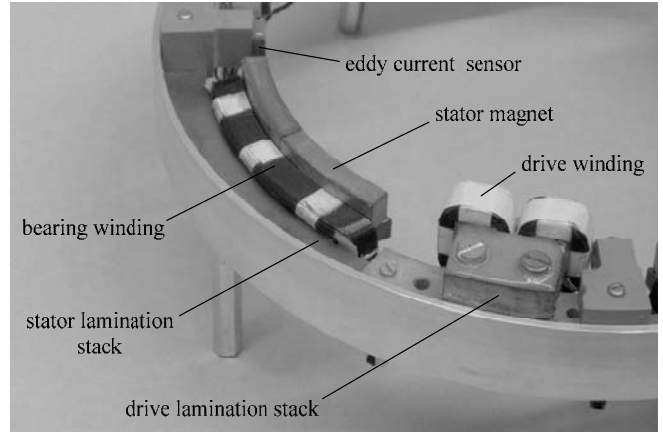


Fig. 9. Detailed view of the experimental set-up with the motor stator and its components.

been realized (see **Fig. 10** and **Fig. 9**, and its key data in **Tab. 2**) and its rotor acceleration time from 0 up to 1200rpm successfully optimized according to the guidelines given in this section.

IV. CONCLUSIONS

This paper briefly describes a novel and compact design concept for contactless levitation and rotation of a rotor through the walls of a process chamber. In the proposed set-up, a homopolar magnetic bearing biased by permanent magnets is combined with a high-pole-number segment motor.

The large width of the air gap and the drive configuration result in a weak magnetic coupling of rotor and stator. Thus, the drive design requires a compromise between a large induced voltage and a small number of turns of the drive windings, since a large inductance combined with a high

number of poles leads to a major inductive voltage drop. Particularly, a motor supplied by a converter with a low dc-link voltage has a reduced maximum possible drive current already at a comparatively low rotor speed. An optimization with respect to the maximum achievable acceleration leads therefore to a moderate torque in the low-speed range.

REFERENCES

- [1] R. Schöb, N. Barletta, M. Weber and R. von Rohr, "Design of a Bearingless Bubble Bed Reactor", Proc. 6th International Symposium on Magnetic Bearings, Cambridge, USA, 1998, pp. 507-516.
- [2] www.semiconductor-manufacturing.net.
- [3] S. Silber, W. Amrhein, P. Bösch, R. Schöb and N. Barletta, "Design Aspects of a Bearingless Slice Motor", IEEE/ASME Transactions on Mechatronics, Volume 10, Issue 6, pp. 611-617, 2005.
- [4] P. Bösch and N. Barletta, "High Power Bearingless Slice Motor (3-4 kW) for Bearingless Canned Pumps", 9th International Symposium on Magnetic Bearings, Lexington, Kentucky, USA, 2004.
- [5] T. Ohishi, Y. Okada, and K. Dejima, "Analysis and Design of a Concentrated Wound Stator for Synchronous-Type Levitated Rotor", 4th International Symposium on Magnetic Bearings, Zürich, 1994.
- [6] A. Chiba, D.T. Power and M.A. Rahman, "Characteristics of a Bearingless Induction Motor", IEEE Transactions on Magnetics, Vol. 27, No.6, Nov. 1991.
- [7] R. Schöb and J. Bichsel, "Vector control of the bearingless motor", 4th International Symposium on Magnetic Bearings, Zürich, 1994.
- [8] M.A. Ooshima et al., "Design and Analysis of Permanent Magnet-Type Bearingless Motors", IEEE Transactions on Industrial Electronics, Vol. 43, No. 2, 1996.
- [9] N. Barletta and R. Schöb, "Design of a Bearingless Blood Pump", 3rd International Symposium on Magnetic Suspension Technology, Tallahassee, FL, 1995.
- [10] J. Zhang, J.O. Schulze and N. Barletta, "Synchronous Three-Level PWM Power Amplifier for Active Magnetic Bearings", 5th International Symposium on Magnetic Bearings, Kanazawa, Japan, 1996.

Inside rotor diameter	160mm
Mechanical air gap	3mm
Maximal torque	0.5Nm
Maximal axial load	47N
Radial load	35N
Axial stiffness	20N/mm
Tilting stiffness	1.1Nm/°
Number of pole pairs	22
Number of bearing coils	4
Number of drive coils	8
Maximal speed	1200rpm
Resistance of one drive coil ($N = 190$)	0.75Ω
Inductivity of one drive coil ($N = 190$)	12mH
In one drive coil induced voltage	6.225mV/rpm

Tab. 2. Key data of the experimental set-up